

**Turbulence statistics and coherent structures in compressible channel flow**Jie Yao \* and Fazle Hussain †*Department of Mechanical Engineering, Texas Tech University, Lubbock, Texas 79409, USA*

(Received 18 April 2020; accepted 2 July 2020; published 7 August 2020)

Direct numerical simulations of compressible turbulent channel flows are performed for bulk Mach numbers 0.8 and 1.5 and bulk Reynolds numbers in the range of 3000–34 000. The compressibility effects are well accounted for when using the semilocal scaling, as expected. Compared to incompressible flows at comparable semilocal Reynolds number  $Re_{\tau_c}^*$ , the mean velocity profile perfectly collapses after the Trettel and Larsson transformation [Trettel and Larsson, *Phys. Fluids* **28**, 026102 (2016)]. Furthermore, the Reynolds stresses, such as their peak values and locations, follow similar trends as in incompressible cases. In particular, the Reynolds shear stress peak follows the nonuniversal scaling transition predicted by Chen *et al.* [*J. Fluid Mech.* **871**, R2 (2019)]. Although the streamwise Reynolds stress peak continuously increases with Mach number, this increase becomes smaller as the Reynolds number increases. The streamwise and spanwise velocity spectra reveal that the typical eddy size does not vary with the Mach number when scaled using the local friction velocity and thermodynamic properties. Additionally, the compressibility contribution to the skin friction continuously decreases with Reynolds numbers. These results suggest that incompressible and compressible flows differ little at sufficiently high Reynolds number.

DOI: [10.1103/PhysRevFluids.5.084603](https://doi.org/10.1103/PhysRevFluids.5.084603)**I. INTRODUCTION**

Compressible wall-bounded turbulent flows (CWTFs) are ubiquitous in nature and engineering applications, such as high-speed vehicles, gas turbine blades, and rocket propulsion systems. In such flows, strong variations of thermo-physical properties can occur, which greatly affect the mean velocity and near-wall turbulent structures and make invalid the scaling laws developed for the incompressible flows [1–4].

To understand the effect of compressibility on the flow statistics, scaling, and structures, extensive studies have been done for CWTFs during recent decades. Coleman *et al.* [5] conducted a direct numerical simulation (DNS) of the compressible turbulent channel flows (CTCFs) between two isothermal walls at bulk Mach numbers  $M_b = 1.5$  and 3 and bulk Reynolds number  $Re_b = 3000$  and 4880. They found that, compared with those caused by thermodynamic fluctuations, the compressibility effects caused by the mean property variations were dominant. In addition, the mean density and temperature gradients result in enhanced coherence of near-wall streaks when compared to incompressible cases. Such streak elongation was also observed by Duan *et al.* [4] and Lagha *et al.* [6] for turbulent boundary layers with cooled walls. Huang *et al.* [7] analyzed DNS results of Ref. [5] and found that the difference between Reynolds and Favre averages was small and mainly in the near-wall region. They proposed a semilocal scaling based on the wall shear stress and local flow properties to better collapse the turbulent statistics profiles in the near-wall

\*jie.yao@ttu.edu

†fazle.hussain@ttu.edu

region with the incompressible data. Morinishi *et al.* [8] performed a DNS of CTCFs between adiabatic and isothermal walls and reported that the near-wall streaks are independent of thermal wall boundary conditions if semilocal units are used to compare with incompressible flows. Foysi *et al.* [9] further analyzed the semilocal scaling for Reynolds stresses in CTCFs with isothermal walls. When compared with the incompressible case, they found that the streamwise Reynolds stress increases, while the wall-normal and spanwise Reynolds stresses decrease. They claimed that, although the semilocal scaling provides a better collapse than the wall scaling, the improvement is limited and mainly due to the nonlocal dependence of pressure on density.

One important challenge in CWTFs is to develop proper transformations that collapse the compressible velocity profile into a universal law of the wall. The van Driest transformation [10], which incorporates the mean density variation effect, has been successful in collapsing velocity profiles between the supersonic flows over adiabatic walls and the incompressible flows [11,12]. The success of the van Driest transformation can be attributed to Morkovin's hypothesis, which assumes that, for moderate Mach numbers, the density fluctuations are negligible, and the compressibility effect on turbulence could be accounted for by the mean density variations alone [13]. However, deviations were observed in flows with strong near-wall density and viscosity gradients [3,4,14]. The limitation of the van Driest transformation motivated the development of alternative transformations. Zhang *et al.* [15] derived a Mach-invariant scaling for compressible turbulent boundary layers using a viscosity-weighted transformation, similar to the viscous sublayer transformation adapted to laminar compressible channel flows. Trettel and Larsson [16] investigated the failure of the van Driest transformation for the isothermal wall case and derived a novel mean velocity transformation which can better incorporate the wall-normal density and viscosity gradient effects. By rescaling the Navier-Stokes (N-S) equations using the local mean properties and semilocal friction velocity, Patel *et al.* [2] derived an equivalent mean velocity transform to that of Trettel and Larsson. Later Modesti and Pirozzoli [1] performed a detailed DNS study of Reynolds and Mach number effects on CTCFs. By comparing different compressibility transformations, they concluded that the Trettel and Larsson transformation performs best for collapsing mean velocity profiles. They found that the semilocal transformation by Huang *et al.* [7] performs well for the Reynolds stresses, with the only exception that the streamwise Reynolds stress peak is typically higher than that of the incompressible case.

To quantify the effect of variable density and viscosity on the scaling of mean velocity, turbulence statistics, and near-wall turbulent structures, Patel *et al.* [2,17] performed DNSs of N-S equations under the low Mach number approximation. Unlike the constant-property turbulent flow, where mean velocity and turbulent statistics can be expressed as a function of wall-normal distance and friction Reynolds number  $Re_\tau$ , they demonstrated that, for the variable-property flows, turbulence statistics and near-wall structures strongly depend on the semilocal Reynolds number  $Re_\tau^* \equiv Re_\tau \sqrt{\bar{\rho}/\bar{\rho}_w}/(\bar{\mu}/\bar{\mu}_w)$  (where the overbar and the subscript  $w$  denote Reynolds averaging and wall quantity, respectively). They also examined how turbulence structures are affected by wall heating or cooling. Sciacovelli *et al.* [18] investigated the influence of dense-gas effects on CWTFs and observed that the presence of strong density fluctuations due to the nonstandard sound speed variation does not significantly alter the turbulence structures, and the semilocal scaling proposed by Trettel and Larsson can be well adapted to compare results in high Mach wall-bounded flows of dense gases with those in the incompressible limit.

Although the semilocal scaling can provide an approximate collapse of mean velocity and Reynolds stress profiles, there is yet no universal scaling with respect to Reynolds number. For example, in the incompressible flows, the peak amplitudes of streamwise and spanwise fluctuations increase logarithmically with  $Re_\tau$ . In the present work, we attempt to understand how turbulent statistics and vortical structures depend on the Reynolds number for CWTFs. The rest of the paper is organized as follows. Section II presents the governing equations, numerical scheme, and simulation parameters. Turbulent statistics, scalings, and structures are discussed in Sec. III. Finally, conclusions are drawn in Sec. IV.

## II. NUMERICAL SETUP

### A. Governing equations

The compressible turbulent flow can be described by the N-S equations:

$$\frac{\partial \rho}{\partial t} + \frac{\partial \rho u_i}{\partial x_i} = 0, \quad (1)$$

$$\frac{\partial \rho u_i}{\partial t} + \frac{\partial \rho u_i u_j}{\partial x_j} = -\frac{\partial p}{\partial x_i} + \frac{\partial \sigma_{ij}}{\partial x_j} + f_i, \quad (2)$$

$$\frac{\partial e}{\partial t} + \frac{\partial (e + p)u_j}{\partial x_j} = \frac{\partial \sigma_{ij}u_i - q_j}{\partial x_j} + f_i u_i, \quad (3)$$

where  $\rho$  is the density,  $u_i$  the velocity component,  $p$  the pressure,  $q_j$  the components of the heat flux vector,  $\sigma_{ij}$  the viscous stress tensor, and  $e = \rho(e_s + u_i u_i / 2)$  the total energy per unit mass, which is the sum of internal energy  $e_s$  and kinetic energy. The fluid considered is a perfect gas, with the thermal and caloric equation of state (EOS)  $p = \rho RT$ ; here  $R$  is the universal gas constant per unit gas. The internal energy  $e_s$  is a function of the temperature  $T$  only,  $e_s = c_v T$ , with  $c_v$  the specific heat at constant volume,  $c_v = R/(\gamma - 1)$ ;  $\gamma = c_p/c_v = 1.4$  is the specific heat ratio, and  $c_p$  is the specific heat at constant pressure.

The fluid is Newtonian with the viscous shear stress given as

$$\sigma_{ij} = 2\mu(S_{ij} - \frac{1}{3}S_{kk}\delta_{ij}), \quad (4)$$

where  $S_{ij} = (\partial u_i / \partial x_j + \partial u_j / \partial x_i) / 2$  is the rate of the strain tensor and  $\mu$  is the dynamical viscosity. For gases,  $\mu$  is an increasing function of temperature, whose dependence on  $T$  is given by Sutherland's law:

$$\mu = \mu_0 \frac{T_0 + S}{T + S} \left( \frac{T}{T_0} \right)^{3/2}, \quad (5)$$

where  $\mu_0$  and  $T_0$  are reference values and  $S$  a constant. Throughout,  $S = 110.4$  K and  $T_0 = 293.15$  K [8]. Finally, the heat flux  $q_j$  is modeled through Fourier's law  $q_j = -k \partial T / \partial x_j$ , where  $k = c_p \mu / \text{Pr}$  is the thermal conductivity, with the Prandtl number  $\text{Pr} = 0.72$ .

### B. Numerical method

A DNS of CTCFs is performed with an in-house finite-difference code. The convective terms are discretized with a seventh-order upwind-biased scheme [19,20], and the viscous terms are evaluated with an eighth-order centered scheme. Time integration is done using the low-storage third-order Runge-Kutta scheme. The DNS is carried out in a rectangular box whose sizes in the  $x, y, z$  directions are denoted as  $L_x, L_y, L_z$ . The periodic boundary condition is enforced in the homogeneous wall-parallel directions, and the no-slip and isothermal boundary conditions are employed for velocities and temperature at the walls. The mesh spacing is constant in the wall-parallel direction, and a mapping function is used in the wall-normal direction to cluster mesh points towards the wall to have the first point  $\Delta y_w^+$ . All simulations are initiated with a parabolic velocity profile plus superimposed random fluctuations and with uniform values for the temperature and density. Following standard practice, e.g., Ref. [5], a spatially constant body force  $f_1$  is applied in the streamwise direction in order to enforce constant mass-flow rate in time, and the corresponding power spent is added to the right-hand side of the total energy equation. The solver is validated in Ref. [21] by comparing flow statistics with both the incompressible data set of Ref. [22] and the compressible data set of Ref. [1].

TABLE I. Details of the numerical parameters employed for the present simulations. The computational box size is  $L_x \times L_y \times L_z = 6\pi h \times 2h \times 2\pi h$  ( $h$  is the half channel height) for all cases.  $N_x$ ,  $N_y$ , and  $N_z$  are the numbers of grid sizes in ( $x$ ,  $y$ ,  $z$ ) directions; and  $\Delta x^+$ ,  $\Delta z^+$ ,  $\Delta y_w^+$ , and  $\Delta y_c^+$  are the mesh sizes in wall units.  $\text{Re}_\tau$  is the friction Reynolds number;  $\text{Re}_{\tau_c}^*$  indicates the semilocal Reynolds number  $\text{Re}_{\tau_c}^*$  at the half channel height.  $Tu_\tau/h$  is the total simulation time without transition.

$M_b$	0.8				1.5			
$\text{Re}_b$	3000	7667	17 000	34 000	3000	7667	17 000	34 000
Case	R3KM08	R8KM08	R17KM08	R34KM08	R3KM15	R8KM15	R17KM15	R34KM15
$\text{Re}_\tau$	198	452	909	1692	219	506	1027	1912
$\text{Re}_{\tau_c}^*$	174	397	798	1484	145	337	683	1266
$N_x$	384	768	1536	3072	512	1024	2048	4096
$N_y$	129	193	385	769	129	257	513	1025
$N_z$	192	384	768	1536	256	512	1024	2048
$\Delta x^+$	9.7	11.1	11.2	10.4	8.1	9.3	9.5	8.3
$\Delta z^+$	6.5	7.4	7.4	6.9	5.4	6.2	6.3	5.6
$\Delta y_w^+$	0.47	0.70	0.70	0.65	0.52	0.58	0.59	0.55
$\Delta y_c^+$	6.4	9.8	9.8	9.1	7.1	8.2	8.3	7.8
$Tu_\tau/h$	50.4	23.6	8.6	4.5	45.3	19.8	7.6	4.1

### C. Simulation parameters

DNS is conducted at four bulk Reynolds numbers (namely,  $\text{Re}_b \equiv \rho_b U_b h / \mu_w = 3000, 7667, 1700,$  and  $34\,000$ ) and two bulk Mach numbers (subsonic  $M_b \equiv U_b / c_w = 0.8$  and supersonic  $1.5$ ), where  $\rho_b$  is the bulk density,  $U_b$  is the bulk velocity,  $\mu_w$  is the dynamic viscosity on the wall, and  $c_w$  is the speed of sound at the wall temperature. For all cases, the computational domain has dimensions  $L_x \times L_y \times L_z = 6\pi h \times 2h \times 2\pi h$ , with  $h$  the half channel height. The mapping function  $y/h = \tanh[B\xi] / \tanh(B)$  with  $\xi \in [-1, 1]$  and  $B = 2$  is employed in the wall-normal coordinate to ensure that the first point in wall unit is less than 1. Details of the simulation parameters (grid sizes, resolutions, and time intervals for the collection of the flow statistics, etc.) are given in Table I. The grid resolution employed here is nearly the same as that used by Modesti and Pirozzoli [1], who demonstrated the sufficiency of this resolution with a detailed sensitivity study.

The quantities nondimensionalized with the wall friction velocity  $u_\tau = \sqrt{\tau_w / \rho_w}$  and the viscous length scale ( $\delta_v = \nu_w / u_\tau$ , where  $\nu = \mu / \rho$  is the kinematic viscosity) are denoted with the superscript  $+$ . The friction Reynolds number is defined as the ratio of outer to viscous length scales, hence  $\text{Re}_\tau = h / \delta_v = u_\tau h / \nu_w$ . Huang *et al.* [7] suggested that normalizing the mean velocity and Reynolds stress profiles with respect to suitable semilocal wall units based on the local density and viscosity (i.e.,  $u_\tau^* = \sqrt{\tau_w / \bar{\rho}}$ ,  $\delta_v^* = \bar{\nu} / u_\tau^*$ ) yields better collapse of the flow statistics with incompressible flows. Accordingly, the semilocal Reynolds number is defined as  $\text{Re}_{\tau_c}^* = h / \delta_v^* = \text{Re}_\tau \sqrt{(\bar{\rho} / \bar{\rho}_w)} / (\bar{\mu} / \bar{\mu}_w)$ . Note that for the isothermal CTCF,  $\text{Re}_{\tau_c}^* = \text{Re}_\tau$  at the wall and decreases towards the channel center. In the present work, both the Reynolds (represented by  $\bar{\phi}$ ) and the Favre averaging ( $\tilde{\phi} = \overline{\rho\phi} / \bar{\rho}$ ) are employed, with  $\phi'$  and  $\phi''$  denoting their remaining fluctuations.

For comparison, the incompressible DNS data by Lee and Moser [22] at  $\text{Re}_\tau = 180, 550, 1000,$  and  $2000$  are employed. They was generated using the spectral code POONGBACK, where the incompressible N-S equations are solved using the method of Kim *et al.* [23], in which equations for the wall-normal vorticity and the Laplacian of the wall-normal velocity are time advanced. In the wall-normal direction, a seventh-order B-spline collocation method is used. A low-storage implicit-explicit scheme based on the third-order Runge-Kutta for the nonlinear terms and the Crank-Nicolson for the viscous terms are used for time advance. In addition, several new simulations at similar  $\text{Re}_{\tau_c}^*$  as the R3KM15, R8KM15, and R34KM15 cases ( $\text{Re}_\tau \approx 1200$ ) are performed using the same code. Details of the simulation parameters (i.e., grid sizes and resolutions) are given in Table II.

TABLE II. Details of the numerical discretization employed for the incompressible turbulent channel simulations. The computational box size is  $6\pi h \times 2h \times 2\pi h$  for all cases, and  $N_x$ ,  $N_y$ , and  $N_z$  are the numbers of grid sizes. The cases I2KM00 and I6KM00 are taken from Yao and Hussain [21].

Case	$Re_b$	$Re_\tau$	$N_x \times N_y \times N_z$	$\Delta x^+$	$\Delta y^+$	$\Delta z^+$
I2KM00	2136	141	$384 \times 128 \times 192$	6.9	0.08–3.3	4.6
I6KM00	5882	340	$768 \times 192 \times 384$	8.3	0.12–5.3	5.6
I25KM00	25 000	1221	$1728 \times 512 \times 1024$	13.3	0.02–7.5	7.5

### III. TURBULENT STATISTICS

#### A. Global flow properties

Table III lists the main characteristic values of the DNS results. The results for the low  $Re_b$  cases are in good agreement with previous data [1,5,9]. As the relatively low  $M_b$  considered, the Reynolds number dependence of thermodynamic properties is weak. The average centerline temperature is approximately 1.1 times the wall temperature for the subsonic  $M_b = 0.8$  and 1.4 times for the supersonic  $M_b = 1.5$  cases, which is due to the enhanced viscous heating. In addition, for a given  $M_b$ , the heat flux  $B_q$  decreases with  $Re_b$ , suggesting the flows asymptotically approach the adiabatic cases when  $Re \rightarrow \infty$ .

#### B. Mean velocity profile

When the compressibility effect is present, classical wall unit scaling fails in collapsing the velocity profiles. Several endeavors have been made to develop transformations that could collapse the compressible velocity into a universal law of the wall. To incorporate the effect of mean density variation, the van Driest transformation [10],

$$U_D^+(y) = \int_0^{U^+} \sqrt{\frac{\bar{\rho}}{\bar{\rho}_w}} dU^+, \quad (6)$$

has typically been employed to collapse velocity profiles of supersonic flows with those of incompressible flows. This transformation works well in collapsing velocity profiles of supersonic

TABLE III. DNS results for global parameters:  $Re_c = \bar{\rho}_c \bar{U}_c h / \bar{\mu}_c$  is the centerline Reynolds number;  $\bar{\rho}_w / \rho_b$  and  $\bar{\rho}_c / \rho_b$  the wall and centerline normalized density;  $\bar{T}_c / T_w$  the centerline temperature;  $M_c = u_c / c_c$  the centerline Mach number;  $\bar{T}_r = T_c [1 + (\gamma - 1) r M_c^2 / 2]$  the recovery temperature;  $M_{\tau_w} = u_\tau / c_w$  the friction Mach number;  $C_f = 2\tau_w / (\rho_b U_b^2)$  the skin-friction coefficient; and  $B_q = \bar{q}_w / (c_p \bar{\rho}_w u_\tau T_w)$  the heat flux at the walls.

$M_b$	0.8				1.5			
$Re_b$	3000	7667	17 000	34 000	3000	7667	17 000	34 000
Case	R3KM08	R8KM08	R17KM08	R34KM08	R3KM15	R8KM15	R17KM15	R34KM15
$Re_c$	3208	8083	17 788	35 092	2699	6844	15 020	29 641
$\bar{\rho}_w / \rho_b$	1.10	1.11	1.11	1.11	1.37	1.37	1.38	1.38
$\bar{\rho}_c / \rho_b$	0.99	1.00	1.00	1.00	0.98	0.99	0.99	0.99
$\bar{T}_c / T_w$	1.11	1.11	1.11	1.11	1.39	1.39	1.39	1.39
$T_w / T_r$	0.79	0.79	0.80	0.80	0.53	0.53	0.52	0.52
$M_c$	0.89	0.87	0.86	0.85	1.49	1.47	1.45	1.43
$10^2 M_{\tau_w}$	4.79	4.27	3.87	3.60	8.03	7.22	6.58	6.10
$10^3 C_f$	7.92	6.29	5.17	4.47	7.84	6.35	5.30	4.57
$-10^2 B_q$	1.51	1.33	1.21	1.13	4.75	4.26	3.92	3.66

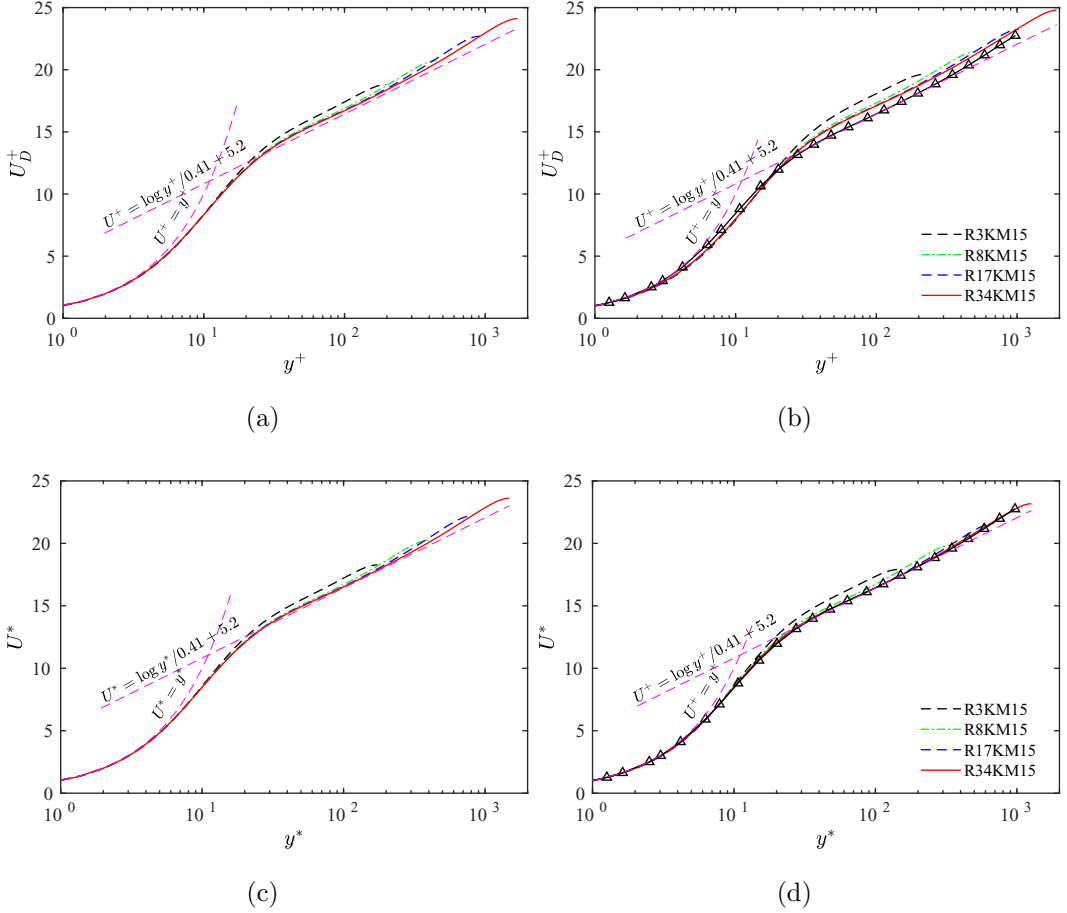


FIG. 1. Mean velocity profiles transformed according to (a), (b) van Driest [10] and (c), (d) Trettel and Larsson [16] for  $M_b = 0.8$  (left) and 1.5 (right). The dashed lines represent the law of the wall: linear law  $U^+ = y^+$  and log law  $U^+ = (1/\kappa) \ln y^+ + B$ , where  $\kappa = 0.41$  and  $B = 5.2$ . The symbol  $\Delta$  in panels (b) and (d) refers to the incompressible I25KM00 case.

flows over adiabatic walls [4,24,25]. However, it fails for flows over diabatic walls, especially for strong heat flux cases [4]. Figures 1(a) and 1(b) show the mean velocity profiles based on van Driest transformation for  $M_b = 0.8$  and 1.5 cases, respectively. The profile for the incompressible flow at  $Re_\tau^* = Re_\tau \approx 1200$  is also compared in Fig. 1(b). Also shown is the law of the wall:  $U^+ = y^+$  and  $U^+ = (1/\kappa) \ln y^+ + B$ , with  $\kappa = 0.41$  and  $B = 5.2$ . Consistent with the previous results [1,2], the van Driest transformation yields the correct log layer profile, but it undershoots the incompressible velocity profile in the viscous sublayer and overshoots in the log layer, especially for the  $M_b = 1.5$  cases. On the other hand, the difference between the van Driest transformed and incompressible velocity profiles becomes smaller for larger  $Re_b$  cases, as the heat flux is reduced.

To better collapse mean velocity profiles for supersonic channel flows with isothermally cooled walls, Trettel and Larsson [16] derived a transformation incorporating the wall-normal density and viscosity gradients

$$U^*(y) = \int_0^{U^+} \sqrt{\frac{\bar{\rho}}{\bar{\rho}_w}} \left( 1 + \frac{1}{2\bar{\rho}} \frac{d\bar{\rho}}{dy} y - \frac{1}{\bar{\mu}} \frac{d\bar{\mu}}{dy} y \right) dU^+. \quad (7)$$

Figures 1(c) and 1(d) further show the mean velocity profiles for  $M_b = 0.8$  and 1.5 cases based on the Trettel and Larsson transformation. Note that the wall-normal distance is nondimensionalized using the semilocal scaling  $y^*(=y\text{Re}_\tau^*)$ . Apparently, the limitation of the van Driest's is overcome by this transformation. The transformed mean velocity  $U^*$  agrees with the incompressible case across the whole wall-normal range. The semilocal scaling  $y^*$  is employed from hereafter as the standard scaling for comparing the incompressible and compressible cases.

The agreements between the Trettel and Larsson transformed and the incompressible velocity profiles suggest that numerous analytical models developed for incompressible flows to predict the mean flow properties [26,27] are still applicable. Let us take the outer layer of the flow as an example. The mean momentum balance equation in turbulent channel flows is

$$\bar{\mu} \frac{d\tilde{u}}{dy} - \bar{\rho} \widetilde{u''v''} = \bar{\rho}_w u_\tau^2 (1 - \eta), \quad (8)$$

where  $\eta = y/h$  is the outer-scaled coordinate. The Reynolds stress can be expressed in terms of an eddy viscosity  $\nu_T$  and velocity gradient:

$$-\widetilde{u''v''} = \nu_T \frac{d\tilde{u}}{dy}. \quad (9)$$

Based on the idea that outer-layer turbulent eddies are not directly affected by the presence of the wall, and their size should hence scale with the channel height and with the typical eddy velocity scale, Pirozzoli [28] suggested that the eddy viscosity can be assumed as  $\nu_T = c_\mu u_\tau^* h$ , where  $c_\mu$  is a suitable constant. Substituting Eq. (9) into (8) and neglecting the viscosity term yields

$$\frac{d\tilde{u}^+}{d\eta} = \frac{1}{c_\mu} \left( \frac{\bar{\rho}_w}{\bar{\rho}} \right)^{1/2} r, \quad (10)$$

with  $r = 1 - \eta$ . Hence the van Driest transformed velocity should follow a parabolic law in the core layer of the channel [1]

$$U_D^+ = U_{Dc}^+ - \frac{1}{2c_\mu} r^2, \quad (11)$$

where  $U_{Dc}^+$  is the transformed centerline velocity.

Recently, She *et al.* [26] proposed a symmetry-based approach to analytically predict mean flow quantities in incompressible wall-bounded turbulent flows. Here we extend it for CWTFs. The Reynolds shear stress can be expressed in terms of the velocity gradient using the mixing-length theory as

$$-\widetilde{u''v''} = \ell_{uv}^2 \left( \frac{d\tilde{u}}{dy} \right)^2, \quad (12)$$

with  $\ell_{uv}$  the stress length function, whose expression for the outer (core) layer is

$$\ell_{uv} = \frac{\kappa_o}{4} \frac{(1 - r^4)}{(1 + r_c^2)^{1/4}} \left[ 1 + \left( \frac{r_c}{r} \right)^2 \right]^{1/4}, \quad (13)$$

where  $\kappa_o = 0.45$  and the core layer thickness  $r_c = 0.27$ . Note that these two values are obtained through a two-parameter fitting procedure using DNS and experimental mean velocity profile data; see Ref. [26] for more details.

Substituting Eq. (12) into (8), we obtain

$$\frac{d\tilde{u}^+}{d\eta} = \frac{1}{\ell_{uv}} \left( \frac{\bar{\rho}_w}{\bar{\rho}} \right)^{1/2} \sqrt{r}, \quad (14)$$

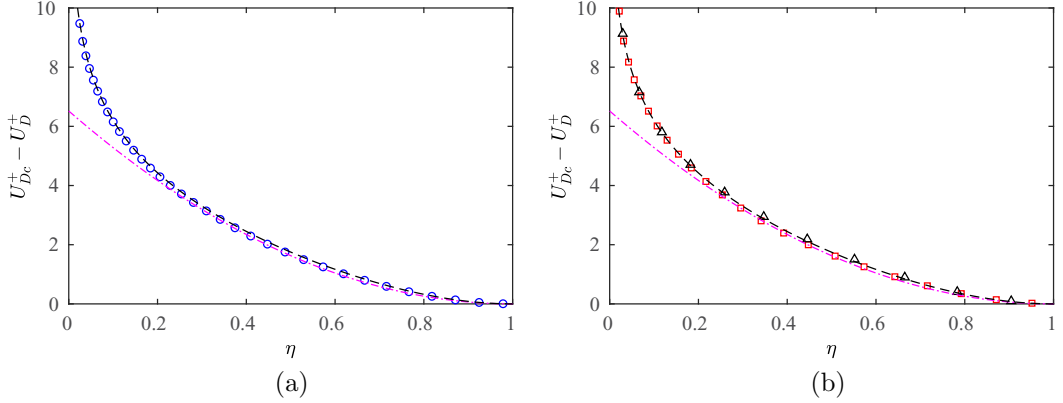


FIG. 2. Van Driest–transformed defect velocity profiles for the (a) R34KM08 (o) and (b) R34KM15 (□) cases. Symbol  $\Delta$  in (b) refers to the incompressible I25KM00 case. The dash-dotted and dashed lines represent Eq. (11) with  $c_\mu = 0.0767$  and Eq. (15) with  $\kappa_o = 0.45$  and  $r_c = 0.27$ .

which gives

$$U_D^+ = U_{Dc}^+ - \int_0^r \frac{\sqrt{r'}}{\ell_{uv}} dr' = U_{Dc}^+ - \int_0^r \frac{4r'[(1+r_c^2)/(r'^2+r_c^2)]^{1/4}}{\kappa_o(1-r'^4)} dr'. \quad (15)$$

Outer defect profiles obtained with the van Driest transformation are shown in Figs. 2(a) and 2(b) for the R34KM08 and R34KM15 cases, respectively. The theoretical predictions obtained based on Eqs. (11) and (15) are also included for comparison. As the effect of viscosity is not important in the outer flow, the van Driest–transformed velocity shows excellent agreement with the incompressible DNS data at similar  $Re_{\tau_c}^*$  throughout the outer layer. Consistent with Ref. [1], the DNS data agree with the prediction of Eq. (11) around the channel centerline, and the range of validity of the parabolic fit extending to about half of the flow domain. Compared with Eq. (11), the prediction based on Eq. (15) yields noticeably better collapse, similar to the finding by Wu *et al.* [29] for compressible turbulent boundary layers.

### C. Mean temperature and velocity relationship

The distribution of the temperature and the associated heat transfer are of great importance in CWTFs. Hence, numerous works have sought quantitative relationships between temperature and velocity through the similarity of momentum and energy transport [7,12,13,30,31]. These theories (referred to as the Reynolds analogy) allow predictions of the wall heat flux, the mean velocity profile, and the skin-friction coefficients based on the compressible velocity transformations [1]. Based on the similarity between the Reynolds averaged momentum and energy equations, Ref. [32] developed the first temperature-velocity relationship for incompressible flows. Then Busemann [33] and Crocco [34] independently obtained a relation (called the Crocco-Busemann relation) for compressible laminar boundary layers by assuming a unity Prandtl number, which was extended to turbulent boundary layers in Ref. [10]. The assumption of a unity Prandtl number is one of the main reasons for the difference between DNS and the Crocco-Busemann relation. To improve this, Walz derived the following temperature-velocity relationship:

$$\frac{T}{T_w} = 1 + \frac{T_r - T_w}{T_w} \frac{\bar{u}}{\bar{u}_c} - r \frac{\gamma - 1}{2} M_c^2 \frac{T_c}{T_w} \left( \frac{\bar{u}}{\bar{u}_c} \right)^2, \quad (16)$$

where  $T_r = T_c[1 + (\gamma - 1)rM_c^2/2]$  is the recovery temperature,  $r = 0.89$  is the recovery factor, and the subscript  $c$  denotes properties at the channel centerline. Similar to the van Driest transformation

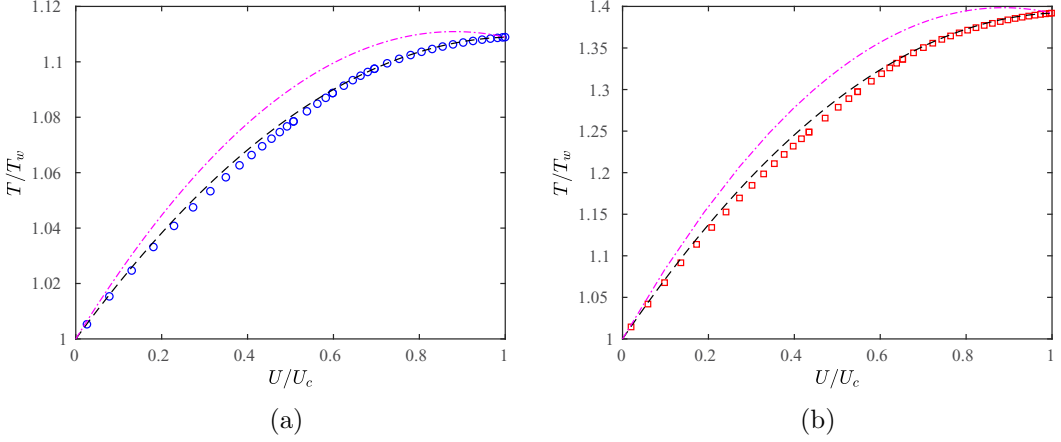


FIG. 3. Mean temperature as a function of mean velocity for the (a) R34KM08 ( $\circ$ ) and (b) R34KM15 ( $\square$ ) compared with Eq. (16) (dashed-dotted lines) and with Eq. (17) (dashed lines).

for the mean velocity, there is good agreement between Eq. (16) and the DNS for boundary layer over adiabatic wall [35] but clear differences for diabatic cases [4].

The limitations of the Walz equation motivated Zhang *et al.* [31] to derive a generalized Reynolds analogy by introducing a general recovery factor:

$$\frac{T}{T_w} = 1 + \frac{T_{rg} - T_w}{T_w} \frac{\bar{u}}{\bar{u}_c} + \frac{T_c - T_{rg}}{T_w} \left( \frac{\bar{u}}{\bar{u}_c} \right)^2, \quad (17)$$

with  $T_{rg} = T_c + r_g u_c^2 / (2C_p)$ ,  $r_g = 2C_p(T_w - T_c) / u_c^2 - 2Prq_w / (u_c \tau_w)$ . It coincides with the Walz relation for the cases of adiabatic walls ( $q_w = 0$ ). Figure 3 compares the DNS data with the prediction of Eqs. (16) and (17). Consistent with the observations in Ref. [1,3], Eq. (17) provides better collapse than Eq. (16). Note that for turbulent channel flows, the centerline values of temperature and velocity are not known *a priori*, thus these temperature-velocity relations cannot be explicitly used to determine the skin coefficients.

#### D. Reynolds stresses

We now examine the Reynolds stress  $\tau_{ij} = \bar{\rho} R_{ij}$ , with  $R_{ij} = \widetilde{u_i'' u_j''} = \widetilde{u_i u_j} - \widetilde{u_i} \widetilde{u_j}$ . Figure 4 shows the Reynolds normal stresses ( $\tau_{11}$ ,  $\tau_{22}$ , and  $\tau_{33}$ ) as a function of the semilocal coordinates  $y^*$ . Similarly to the observation for incompressible flows [22,36], at a fixed  $M_b$ , the Reynolds stresses increase with  $Re_b$ , presumably due to the enhanced influence of outer-layer modes on the near-wall dynamics [37,38]. The locations of the peak values are roughly constant for the streamwise and spanwise components,  $y^* \approx 15$  for  $\tau_{11}$  and  $y^* \approx 40$  for  $\tau_{33}$ , and slightly increase with  $Re$  for the wall-normal component. Again, this behavior is consistent with the incompressible cases [22].

The streamwise Reynolds stress for the compressible flows increases in comparison to the incompressible case at comparable  $Re_{\tau_c}^*$ . The peak of  $\tau_{11}$ , which is assumed to vary with Reynolds number logarithmically [22,39,40], increases with  $M_b$  [Fig. 6(a)]. Similar behavior has been recently reported by Zhang *et al.* [3] in hypersonic turbulent boundary layers. Using the data at the three highest  $Re$  cases, the dependence of the peak in  $\tau_{11}$  on  $Re_{\tau_c}^*$  is fitted to obtain

$$\tau_{11} / \tau_w = A \log(Re_{\tau_c}^*) + B, \quad (18)$$

with  $A = 0.714, 0.615, \text{ and } 0.535$  and  $B = 3.16, 4.24, \text{ and } 5.16$  for the incompressible,  $M_b = 0.8$ , and  $M = 1.5$  cases, respectively. Note that a slightly larger  $A$  value than that reported in Ref. [22] for the incompressible case is due to the low values of  $Re_\tau$  considered. A slower growth rate for higher

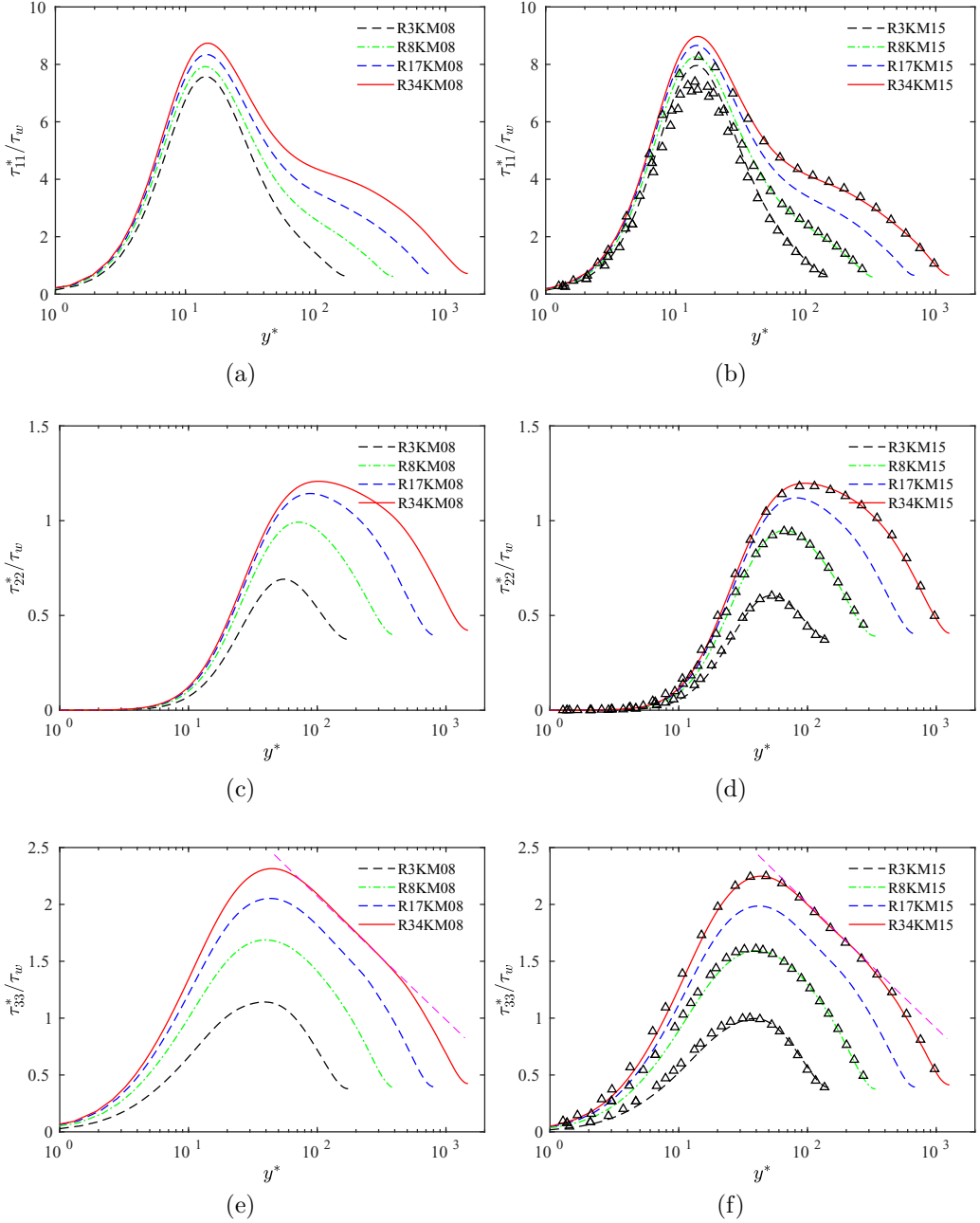


FIG. 4. Reynolds normal stress components as a function of  $y^*$  for (left)  $M_b = 0.8$  and (right) 1.5 cases: (a), (b)  $\tau_{11}$ , (c), (d)  $\tau_{11}$ , (e), (f)  $\tau_{33}$ . The symbol  $\Delta$  in panels (b), (d), and (f) refers to the I2KM00, I6KM00, and I25KM00 cases, and the straight dashed line in panels (e) and (f) denotes  $\tau_{33}^*/\tau_w = 0.8 - 0.47 \log(y/h)$ .

$M_b$  cases suggests that the difference between the incompressible and compressible cases becomes smaller at very high Reynolds numbers. Differently from  $\tau_{11}$ , the  $\tau_{22}$  and  $\tau_{33}$  values overall show good agreement between incompressible and compressible flows at comparable  $\text{Re}_{\tau_C}^*$ , except in the near-wall region, where a slight decrease is observed for the compressible cases. This is consistent with the previous findings by Modesti and Pirozzoli [1] and Duan *et al.* [12].

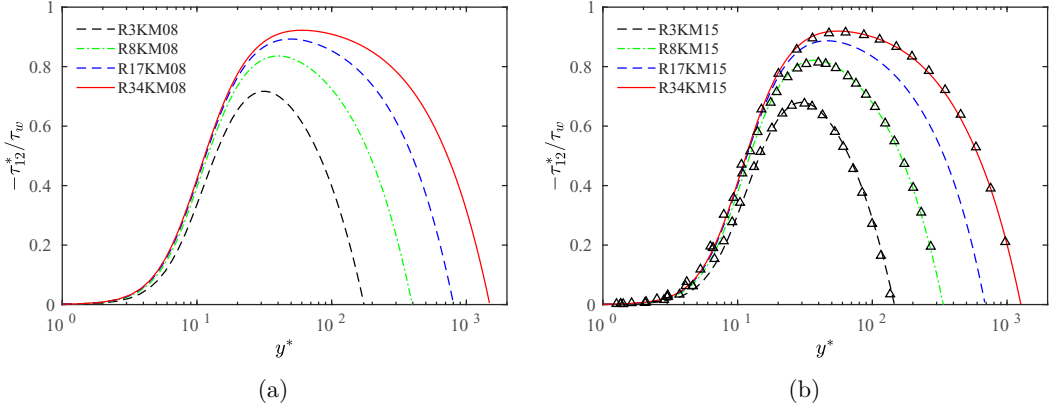


FIG. 5. Reynolds shear stresses  $\tau_{12}$  normalized by the wall shear stress  $\tau_w$  for (a)  $M_b = 0.8$  and (b) 1.5 cases. The symbol  $\triangle$  in (b) refers to the I2KM00, I6KM00, and I25KM00 cases.

Similarly to the log law for the mean velocity, Townsend's attached eddy hypothesis implies that in the high Reynolds number limit, there is an interval in  $y$  in which the streamwise and spanwise Reynolds stresses exhibit logarithmic variations and the wall-normal stress has a plateau [22]. It is clear that, at the Reynolds number considered, there is no apparent range with a logarithmic variation for the streamwise stress. On the other hand, it appears that there is a logarithmic variation for the spanwise component. The fit in the log region for the R34KM15 case gives  $\tau_{33}^*/\tau_w = 0.8 - 0.47 \log(y/h)$ , which is very close to that found by Jimenez and Hoyas [41].

Figure 5 further examines the normalized Reynolds shear stress  $\tau_{12}/\tau_w$  profiles. Similarly to other Reynolds stress components,  $\tau_{12}$  also increases with  $\text{Re}$ , and the peak values  $\tau_{12}^p$  and locations  $y_{12}^p$  both show a weak  $\text{Re}$  dependence. In addition, good collapse is observed between incompressible and supersonic cases at matching  $\text{Re}_{\tau,c}^*$ . At asymptotically high  $\text{Re}_{\tau}$ ,  $y_{12}^p$  is known to exhibit a  $\text{Re}_{\tau}^{1/2}$  scaling [42] for incompressible turbulent channel flow. Recently, Chen *et al.* [43], based on the Lie symmetry approach, showed that  $y_{12}^p$  in wall units displays a scaling transition from  $y_{12}^p \sim 5.7\text{Re}_{\tau}^{1/3}$  to the traditional  $1.5\text{Re}_{\tau}^{1/2}$ ; and correspondingly the peak value also shows a transition from  $\tau_{12}^p \sim 1-8.5\text{Re}_{\tau}^{-2/3}$  to  $1-3.0\text{Re}_{\tau}^{-1/2}$ . Figure 6(b) shows the peak value and locations of  $\tau_{12}$  as a function of  $\text{Re}_{\tau,c}^*$  for all  $M_b$  cases; also included are the theoretical prediction given by Chen *et al.* [43]. It is clear that the peaks  $\tau_{12}^p$  collapse among different  $M_b$  cases and closely follow the nonuniversal scaling transition [43]. Also, for the Reynolds number considered, the peak location  $y_{12}^p$  agrees well with  $\text{Re}_{\tau,c}^{1/3}$  scaling.

### E. Skin friction and its decomposition

The mean skin-friction coefficient  $C_f$  as a function of  $\text{Re}_{\tau}$  is shown in Fig. 7(a). They are compared to the incompressible DNS results and the empirical correlation proposed by Abe and Antonia [44],  $C_f = 2/[2.54/\ln(\text{Re}_{\tau}) + 2.41]^2$ . For a given  $\text{Re}_{\tau}$ , the computed  $C_f$  values for compressible flows are slightly larger than the incompressible cases. Note that the thermodynamic property variations cannot be fully taken into account when using the semilocal Reynolds number  $\text{Re}_{\tau,c}^*$  [Fig. 7(b)]. For a given  $\text{Re}_{\tau,c}^*$ ,  $C_f$  decreases with increasing  $M_b$ , but follows closely the trend as predicted by Ref. [44]. Several compressibility corrections have been proposed for the turbulent boundary layers over adiabatic walls [45,46]. However, these cannot be easily extended to channel flows, as the free-stream (centerline) values strongly depend on Reynolds and Mach numbers. Nevertheless, it is clear from Fig. 7(b) that the compressibility effect decreases with  $\text{Re}_{\tau,c}^*$ . Similar behavior has also been reported [47] for the  $M_b = 3.0$  case. Hence, we speculate that the empirical correlation developed for incompressible flows can be applied at sufficiently high  $\text{Re}_{\tau,c}^*$ .

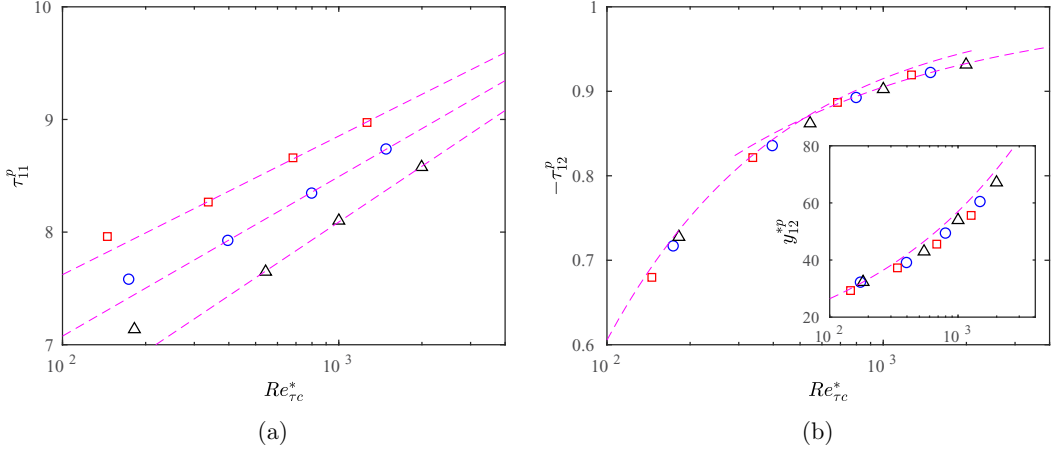


FIG. 6. Peak values of (a)  $\tau_{11}$  and (b)  $\tau_{12}$  as a function of  $Re_{\tau_c}^*$ . The dashed lines in (a) denotes  $\tau_{11}^p/\tau_w = A \log(Re_{\tau_c}^*) + B$  scaling and in (b) represent  $\tau_{12}^p/\tau_w = 1 - 8.5Re_{\tau_c}^{*-2/3}$  and  $1 - 3.0Re_{\tau_c}^{*-1/2}$ . The inset in (b) shows the peak location  $y^p$  of  $\tau_{12}$ , with the dashed line indicating  $y^p \sim 5.7Re_{\tau_c}^{*1/3}$ .

The mean skin-friction  $C_f$  can be further decomposed into different physics-informed contributions based on the mean and statistical turbulence quantities across the wall layer. With integration of the mean momentum balance equation, Fukagata *et al.* [48] derived a relationship (also referred to as the FIK identity) between the  $C_f$  and the Reynolds shear stress for incompressible flows. The FIK identity was extended to compressible flows by Gomez *et al.* [49], which reads as

$$C_f = \underbrace{\frac{6}{Re_b}}_{c_f^L} + \underbrace{6 \int_0^1 (1-y) \overline{\rho - u''v''} dy}_{c_f^T} + \underbrace{\frac{6}{Re_b} \int_0^1 (1-y) \left(1 - \frac{\bar{\mu}}{\bar{\mu}_w}\right) \frac{\partial \bar{u}}{\partial y} dy}_{c_f^M} + \underbrace{\frac{6}{Re_b} \int_0^1 -(1-y) \overline{\mu' \left( \frac{\partial u'}{\partial y} + \frac{\partial v'}{\partial x} \right)} dy}_{c_f^{M^T}}.$$

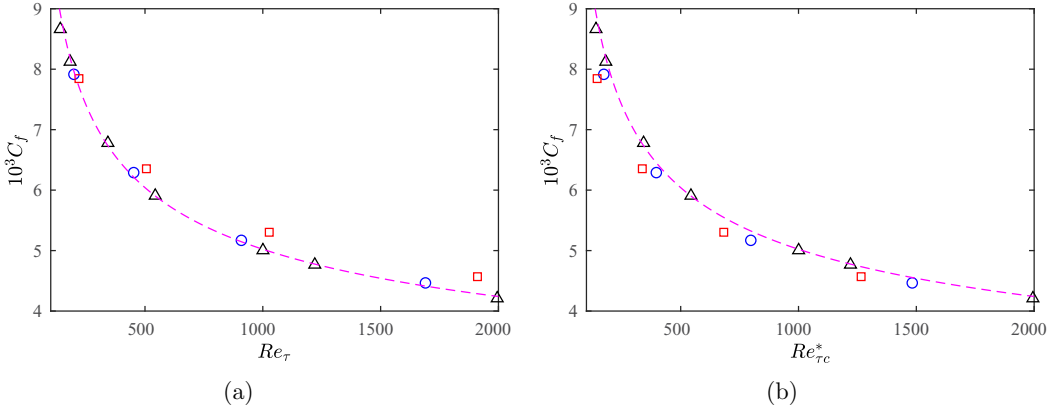


FIG. 7. Mean skin-friction coefficient  $C_f$  as a function of (a)  $Re_{\tau}$  and (b)  $Re_{\tau_c}^*$ . The symbols  $\Delta$ ,  $\circ$ , and  $\square$  refer to the incompressible,  $M_b = 0.8$ , and  $1.5$  cases, respectively. The dashed line denotes the empirical correlation  $C_f = 2/[2.54/\ln(Re_{\tau}) + 2.41]^2$ .

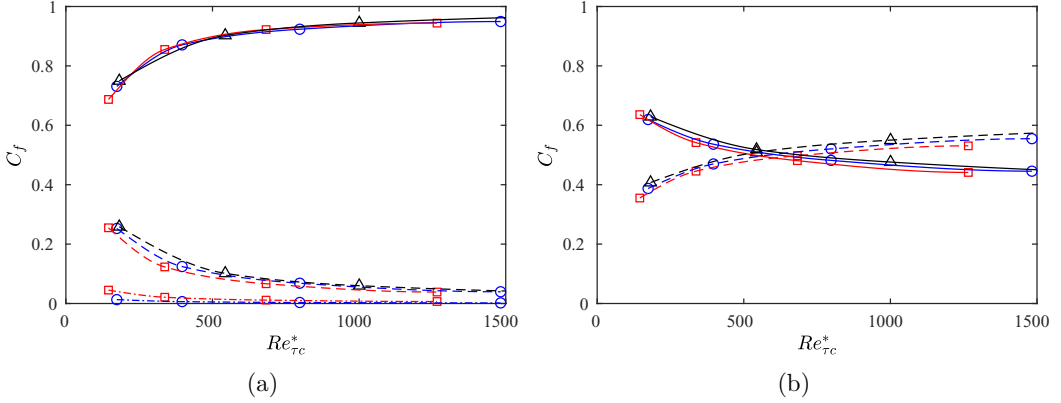


FIG. 8. Mean skin-friction decomposition as a function of  $Re_{\tau c}^*$  for (a) FIK and (b) RD identities. The symbols  $\Delta$ ,  $\circ$ , and  $\square$  refer to the incompressible,  $M_b = 0.8$ , and 1.5 cases, respectively.

The skin friction is decomposed into four components: an “equivalent” laminar part  $C_f^L$ , a turbulent part  $C_f^T$  represented by the weighted integration of the total Reynolds shear stress, the compressible contribution  $C_f^\mu$  related to the mean viscosity variations and the mean wall-normal velocity gradient, and the compressible-turbulent interaction part  $C_f^{\mu T}$ .

The decomposed skin-friction ( $C_f^L$ ,  $C_f^T$ ,  $C_f^\mu$ ) components normalized by the total  $C_f$  as a function of  $Re_{\tau c}^*$  are depicted in Fig. 8(a). Note that the compressible-turbulent interaction term  $C_f^{\mu T}$ , which is typically very small even at high Mach numbers [50,51], is neglected. Similarly to the trend observed for incompressible flows [52,53],  $C_f^L/C_f$  decreases with increasing  $Re_{\tau c}^*$ . The compressible contribution  $C_f^\mu$  related to the mean viscosity variations also decreases with  $Re_{\tau c}^*$ . Additionally,  $C_f^L/C_f$  is found to decrease with increasing  $M_b$ , while  $C_f^\mu/C_f$  increases with  $M_b$ . Interestingly,  $C_f^T/C_f$ , which continuously increases with  $Re_{\tau c}^*$ , is not significantly influenced by  $M_b$ , akin to the observation in Ref. [51]. Hence, at very high Reynolds numbers, the turbulent term  $C_f^T$  is still the dominant contribution to the total  $C_f$ , which should be the main focus for drag control. Based on the Helmholtz decomposition, Yu *et al.* [51] further split  $C_f^T$  into the contributions from solenoidal velocity fluctuations, from dilatational velocity fluctuation, and from their cross-correlation. They found that the correlation term accounts for a non-negligible fraction to the total  $C_f$  at high  $M_b$ .

The FIK identity has several drawbacks. One of the key issues is that there is no physical interpretation for the linearly weighted Reynolds shear stress. Recently, an alternative mean skin-friction decomposition was proposed by Renard and Deck [54], referred to as the RD identity. The RD identity, which was derived from the mean streamwise kinetic-energy equation in an absolute reference frame, characterizes the power of skin friction as an energy transfer from the wall to the fluid by means of the dissipation of molecular viscosity and turbulent production. It was extended to compressible flow by Ref. [47], which reads as

$$C_f = 2 \underbrace{\int_0^1 \overline{\mu \left( \frac{\partial u}{\partial y} + \frac{\partial v}{\partial x} \right) \frac{\partial \tilde{u}}{\partial y}} dy}_{C_f^M} + 2 \underbrace{\int_0^1 \overline{\rho u' v'} \frac{\partial \tilde{u}}{\partial y} dy}_{C_f^P}. \quad (19)$$

Consistent with the incompressible RD identity,  $C_f^M$  and  $C_f^P$  denote the molecular viscous dissipation and turbulent production, respectively. In compressible flows, the viscous dissipation term  $C_f^M$  can

be further decomposed as

$$C_f^M = 2 \underbrace{\int_0^1 \bar{\mu} \frac{\partial \bar{u}}{\partial y} \frac{\partial \tilde{u}}{\partial y} dy}_{C_f^{M1}} + 2 \underbrace{\int_0^1 \mu' \left( \frac{\partial u'}{\partial y} + \frac{\partial v'}{\partial x} \right) \frac{\partial \tilde{u}}{\partial y} dy}_{C_f^{M2}}, \quad (20)$$

which depends on the mean flow and thermodynamic fluctuations, respectively.

Figure 8(b) shows the decomposed skin friction ( $C_f^{M1}$ ,  $C_f^P$ ) normalized by the total  $C_f$  as a function of  $\text{Re}_{\tau_c}^*$  for different  $M_b$  cases. Again, for the  $M_b$  considered here, the compressible-turbulent interaction term  $C_f^{M2}$  is very small, thus not included. As expected, with increasing  $\text{Re}_{\tau_c}^*$ , the contribution from  $C_f^{M1}$  continuously decreases and from  $C_f^P$  increases, and  $C_f^P$  overtakes  $C_f^{M1}$  around  $\text{Re}^* \approx 500$ . At the same  $\text{Re}_{\tau_c}^*$ , varying the bulk Mach number  $M_b$  from 0.8 to 1.5 does not have significant influence on the decomposed results. To quantify the effect of density and viscosity variations on the skin friction, Li *et al.* [47] further employ the van Driest transformation to separate the “incompressible” and “compressible contributions. They found that the incompressible contribution is comparable to the equivalent terms in incompressible turbulent channel flows, and the compressible contribution becomes negligible at sufficient large  $\text{Re}_{\tau_c}^*$ .

## F. Energy spectra

Energy spectra provide information on how the turbulence intensity is distributed across wave numbers and have been widely used to understand the turbulence cascade [55,56]. Figure 9 shows the premultiplied streamwise spectra  $k_x E_{uu}/\tau_w$  and  $k_x E_{uv}/\tau_w$  in semilocal units for the R34KM08 and R34KM15 cases, along with the incompressible I25KM00 case. Note that to highlight the eddies’ length scales, we show wavelength  $\lambda_x^* = 2\pi/k_x^*$ , rather than the corresponding wave numbers, on the horizontal axis. Compared with the wall unit scaling [17,21] the semilocal scaling yields a good collapse over a wide range of  $\lambda_x^*$  and  $y^*$ . The inner-layer spectra clearly show the presence of an energetic inner site corresponding to the near-wall streak generation cycle [57,58]. For the streamwise velocity, a universal inner peak is observed at  $y^* \approx 15$  with  $\lambda_x^* \approx 1000$ , which corresponds to the typical length of near-wall streaks—not very different from incompressible cases. Figure 10 further displays the premultiplied spanwise spectra  $k_z E_{uu}/\tau_w$  and  $k_z E_{uv}/\tau_w$ . Again, good agreements can be observed between the incompressible and compressible cases. The typical length scale for the inner peak remains roughly universal in the spanwise direction, namely,  $\lambda_z^* \approx 110$ , the typical size of the streak spacing. In addition, one important property of wall-bounded turbulence at high Reynolds numbers is the scale separation between the near-wall and outer layers [22]. This scale separation can be seen clearly in  $k_z E_{uu}/\tau_w$ , where an outer peak is located at  $200 \leq y^* \leq 300$  and  $1000 \leq \lambda_z^* \leq 2000$ . Although the scale of the energy-containing motions is increased when compared with the spectrum at low Reynolds number [23,59], the dual peaks have not yet been observed in the  $uv$  cospectrum.

One-dimensional premultiplied spectra for the streamwise velocity components are further shown in Figs. 11(a) and 11(b) for the inner layer  $y^* = 15$  and [Figs. 11(c) and 11(d)] for the outer layer  $y/h = 0.3$ . Note that other velocity components show good agreement between the incompressible and compressible cases and hence are not shown. Compared with the incompressible cases,  $k_x E_{uu}$  for  $y^* = 15$  is slightly enhanced at the large streamwise wavelength for the compressible cases, causing a larger peak of the streamwise Reynolds stress in Fig. 4(b). As expected, for  $y^* = 15$ ,  $k_z E_{uu}$  displays a distinct peak, located at  $\lambda_z^* \approx 110$  and is almost invariant with the Reynolds and Mach numbers. In addition, energy at large spanwise wavelength continuously increases with  $\text{Re}_{\tau_c}^*$ . For the R34KM15 case, a second peak starts to develop at  $\lambda_z^* \approx 1500$ , similarly to the incompressible flows, and is attributed to the footprint of the large-scale and very large-scale motions found in the outer regions [60,61]. Differently from the slight deviation in the near wall, the spectra show better agreement between the incompressible and compressible cases for  $y/h = 0.3$  –

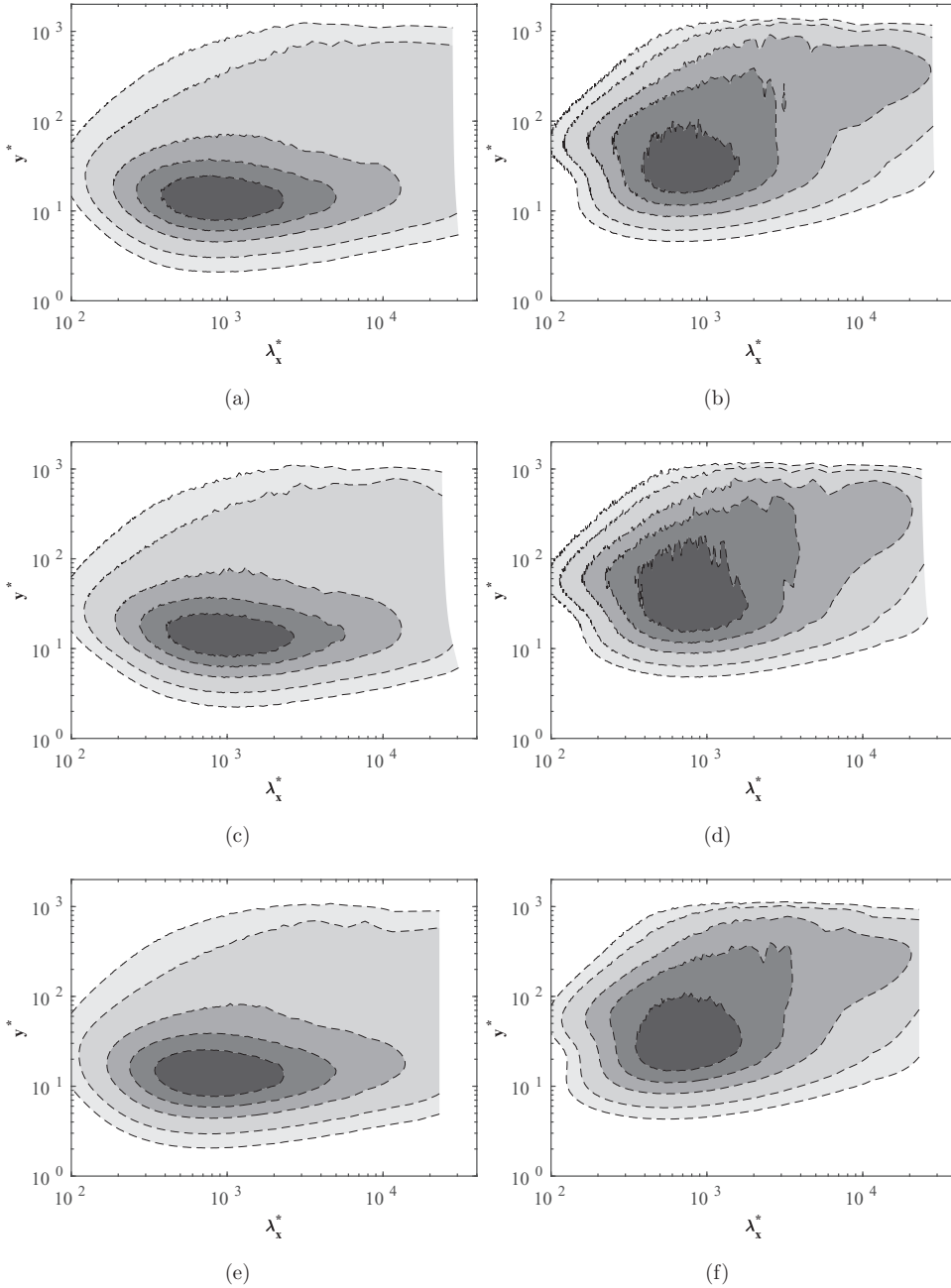


FIG. 9. Premultiplied streamwise spectra of (a), (c), (e) streamwise velocity  $k_x E_{uu}$  and (b), (d), (f)  $k_x E_{uv}$  as a function of streamwise wavelength  $\lambda_x^*$  and  $y^*$ . The panels from top row to bottom row represent yjr R34KM08, R34KM15, and I25KM00 cases, respectively.

consistent with the collapses of the streamwise Reynolds stress in Fig. 4(b). The typical length scales of the eddies at the outer layer are  $\lambda_x/h = 2 \sim 10$  and  $\lambda_z/h \approx 1$ , which suggests a similar presence of large-scale structures as in compressible flows.

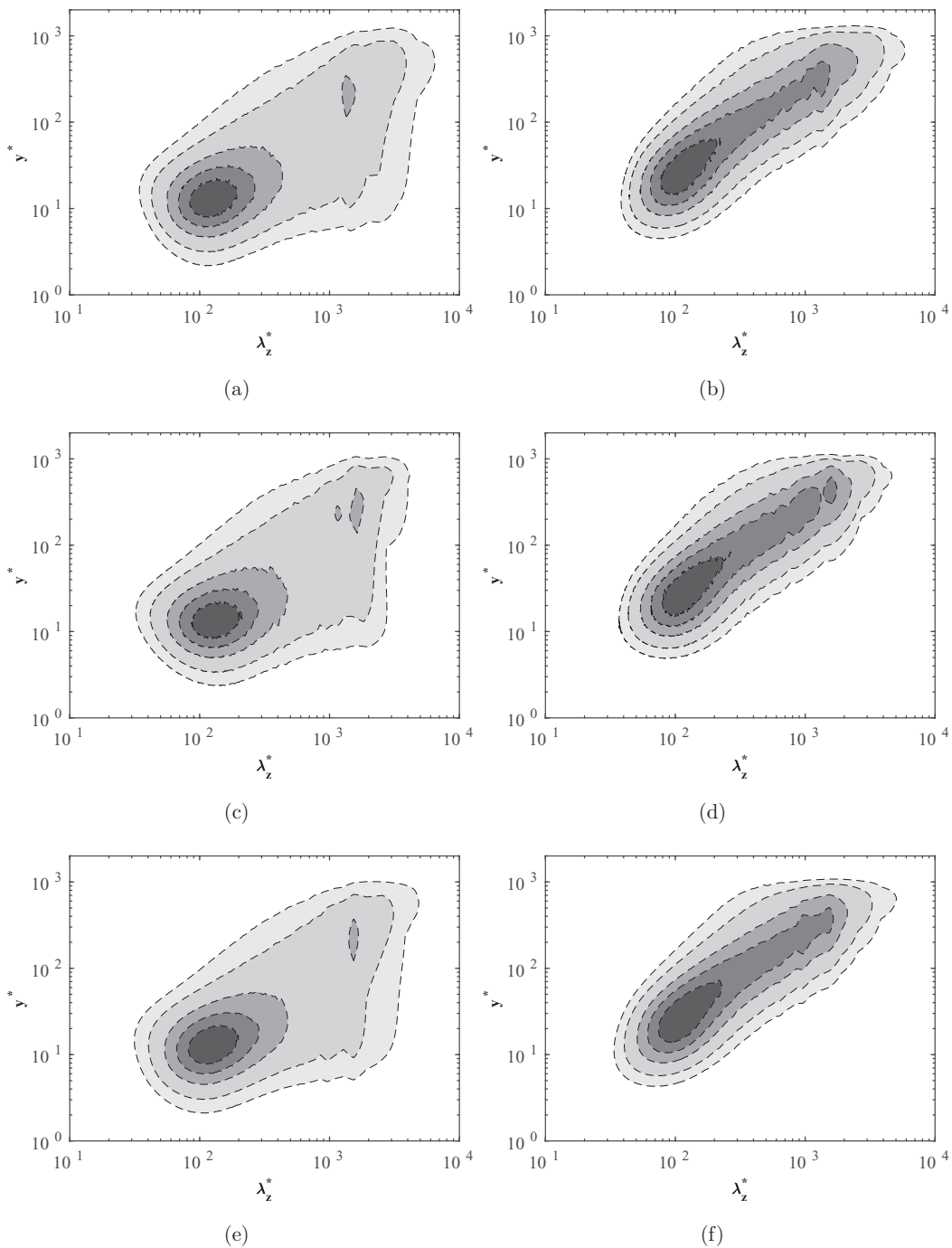


FIG. 10. Premultiplied spanwise spectra of (a), (c), (e) streamwise velocity  $k_z E_{uu}$  and (b), (d), (f)  $k_z E_{uv}$  as a function of spanwise wavelength  $\lambda_z^*$  and  $y^*$ . The panels from top row to bottom row represent the R34KM08, R34KM15, and I25KM00 cases, respectively.

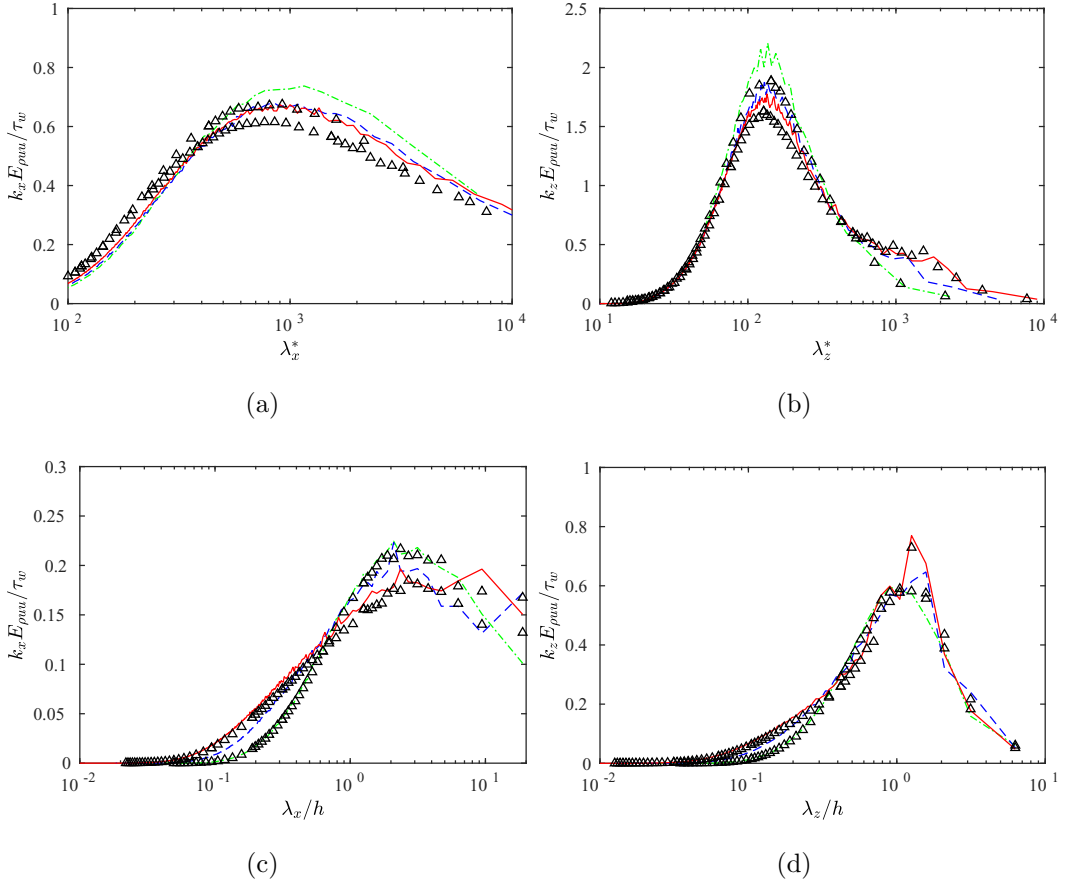


FIG. 11. One-dimensional premultiplied spectra of streamwise velocity at (a), (b)  $y^* = 15$  and (c), (d)  $y/h = 0.3$  for  $M_b = 1.5$  case. The symbol  $\Delta$  refers to the incompressible I6KM00 and I25KM00 cases.

### G. Turbulent structures

Further insights into the flow physics can be obtained by examining the instantaneous velocity and vorticity fields. Figure 12 shows streamwise velocity fluctuations  $\sqrt{\rho} u'' / \sqrt{\tau_w}$  in a plane parallel to the wall for R34KM15 and I25KM00 cases at  $y^* \approx 15$  [Figs. 12(a) and 12(b)] and  $y/h = 0.3$  [Figs. 12(c) and 12(d)], respectively. Similar to Ref. [17], instead of  $\bar{\rho}$ , the local density value  $\rho$  is used for normalization to better accentuate the modulation of the streak magnitude. It was previously argued that the compressibility effect increases the coherence of near-wall streaks for flows with cooled wall [4,5]. However, when the semilocal scaling is employed, a universal behavior seems to emerge [2,18,21]. This is further confirmed here, where, for both cases, the streamwise velocity close to the wall exhibits the organization of the streaks with a spacing of approximately 100. Consistent with previous findings [36,62–64], the outer layer flow exhibits very long regions of negative streamwise velocity fluctuations [visible in Figs. 12(c) and 12(d) as elongated white regions]. Similar to the finding from energy spectra, these structures have characteristic lengths that scale on the outer units, which are about  $\lambda_x \approx 10h$  and  $\lambda_z \approx h$  in the streamwise and spanwise directions, respectively.

Figure 13 shows the top view of instantaneous vortical structures visualized using the  $\lambda_\rho$  criterion [65] for the R34KM15 and I25KM00 cases in the near-wall region ( $y^* \leq 100$ ); also shown are the streaks at  $y^* = 15$ . The distribution of these structures for the two cases is quite similar:

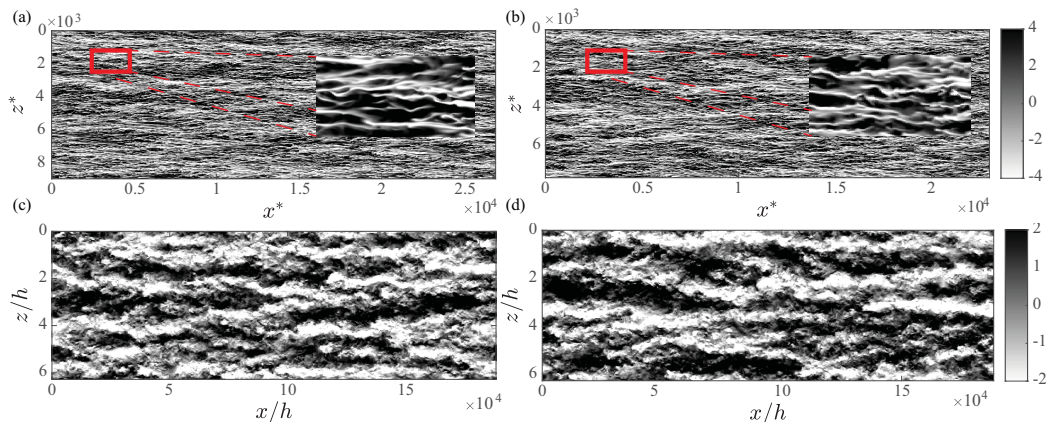


FIG. 12. Instantaneous streamwise velocity fluctuations  $\sqrt{\rho}u''/\sqrt{\tau_w}$  in  $x - z$  planes at (a, b)  $y^* \approx 15$  and (c, d)  $y/h = 0.3$ . The left and right panels represent the R34KM15 and I25KM00 cases, respectively. The insets in (a) and (b) shows a zoom of a  $1500 \times 750$  box in semilocal units.

quasistreamwise vortices dominate the buffer layer, and a few hairpin vortices are observed in the log layer ( $y^* > 50$ ). Note that the role of hairpin vortices in wall-bounded turbulence has remained rather elusive [66,67]. Adrian [66] suggests that the hairpin-type vortices, which can regenerate and form packets, are the fundamental structures in wall-bounded turbulence. On the other hand, several works show that complete hairpin vortices are seldom observed in fully developed turbulence [57,67]. In addition, at high Reynolds numbers, hairpin structures become broken and fragmented [68], hence the log layer might comprise a mix of streamwise and hairpin vortices. To provide further insight into this controversial issue, a robust method that objectively detects and extracts these structures is required [69]. Consistent with the previous studies [64,70], the strengths of these near-wall vortical structures are influenced by the footprint of large-scale motions in the outer layer: they are more intense in the region of large-scale high-speed region, and weaker near the large-scale low-speed regions.

#### IV. CONCLUSIONS

Direct numerical simulations of compressible turbulent channel flows are carried out for  $M_b = 0.8$  and  $1.5$  and  $Re_b$  up to 34 000, along with several incompressible simulations at matching Reynolds numbers. Consistent with the previous studies, the compressibility effects can be

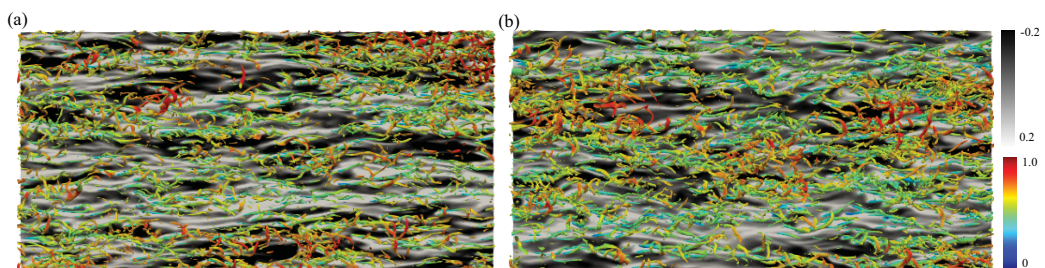


FIG. 13. Top view of instantaneous near wall vortical structures (visualized using  $\lambda_\rho$  criterion for  $y^* \leq 100$ ) shaded with the streamwise velocity  $u/U_b < 1$  for the (a) R34KM15 and (b) I25KM00 cases. Note that the domain size is  $L_x \times L_z = \pi h \times \pi h/2$ , and the streamwise velocity fluctuations  $|\sqrt{\rho}u''/\sqrt{\tau_w}| < 0.2$  at  $y^* \approx 15$  (gray) are also included.

incorporated when using the semilocal scaling. In comparison to the incompressible flows at comparable  $\text{Re}_{\tau_c}^*$ , the mean velocity profiles show perfect collapse when using the Trettel and Larsson transformation. In addition, several analytical modes developed to characterize the mean velocity profiles in the outer layer are examined, and good collapses are observed between the DNS results and these predictions when the local density variations are included using the van Driest transformation.

The behaviors of the Reynolds stresses, such as their peak values and locations, follow the same trends as in incompressible flows. For example, the peak value of the Reynolds shear stresses follows the nonuniversal transition  $y_{12}^p \sim \text{Re}_{\tau}^{1/3}$  to  $\sim \text{Re}_{\tau}^{1/2}$  as found for incompressible flows [43]. For a given  $M_b$ , the peak of the streamwise Reynolds stress varies with Reynolds number logarithmically. Although the peak of the streamwise Reynolds stress continuously increases with Mach number, the differences become smaller at higher Reynolds numbers. The variation of the skin friction and its decomposition based on the compressible versions of the FIK and RD identities are studied. We find that the compressibility contribution to the skin friction continuously decreases with increasing Reynolds numbers.

The streamwise and spanwise spectra of the velocity fields are also scrutinized, and the typical size of the eddies does not vary with the Mach number when scaled on the local friction velocity and flow properties. In particular, the streamwise velocity spectra exhibit a distinct inner peak with  $\lambda_x^* \approx 1000$  and  $\lambda_z^* \approx 110$ . In addition, an outer peak located at  $\lambda_z/h \approx 1$  is revealed for the spanwise spectrum of the streamwise velocity. These observations are further confirmed by visualization of the streamwise velocity fluctuations. The flow phenomena that occur for incompressible high Reynolds number flows, such as the existence of large-scale motions and their modulation of near-wall coherent structures, are also observed for compressible flows. In summary, our results suggest that, at sufficiently high Reynolds numbers, the compressibility effect becomes limited and the flow dynamics become very similar between incompressible and compressible cases. Note that as the Mach numbers considered here are relatively low, DNSs at even higher Mach numbers are required to support this claim.

The flow statistics data are openly available from Texas Data Repository Dataverse [71].

#### ACKNOWLEDGMENTS

Computational resources provided by Texas Tech University HPCC, TACC Lonestar, Frontera under allocation number CTS20008, and XSEDE Stampede2 under allocation number CTS190038 are acknowledged. We also appreciate Lee and Moser for providing us their incompressible DNS code, which is used for this study.

- 
- [1] D. Modesti and S. Pirozzoli, Reynolds and Mach number effects in compressible turbulent channel flow, *Intl. J. Heat Fluid Flow* **59**, 33 (2016).
  - [2] A. Patel, B. J. Boersma, and R. Pecnik, The influence of near-wall density and viscosity gradients on turbulence in channel flows, *J. Fluid Mech.* **809**, 793 (2016).
  - [3] C. Zhang, L. Duan, and M. M. Choudhari, Direct numerical simulation database for supersonic and hypersonic turbulent boundary layers, *AIAA J.* **56**, 4297 (2018).
  - [4] L. Duan, I. Beekman, and M. Martin, Direct numerical simulation of hypersonic turbulent boundary layers. Part 2. Effect of wall temperature, *J. Fluid Mech.* **655**, 419 (2010).
  - [5] G. N. Coleman, J. Kim, and R. Moser, A numerical study of turbulent supersonic isothermal-wall channel flow, *J. Fluid Mech.* **305**, 159 (1995).
  - [6] M. Lagha, J. Kim, J. Eldredge, and X. Zhong, A numerical study of compressible turbulent boundary layers, *Phys. Fluids* **23**, 015106 (2011).
  - [7] P. Huang, G. Coleman, and P. Bradshaw, Compressible turbulent channel flows: DNS results and modelling, *J. Fluid Mech.* **305**, 185 (1995).

- [8] Y. Morinishi, S. Tamano, and K. Nakabayashi, Direct numerical simulation of compressible turbulent channel flow between adiabatic and isothermal walls, *J. Fluid Mech.* **502**, 273 (2004).
- [9] H. Foyisi, S. Sarkar, and R. Friedrich, Compressibility effects and turbulence scalings in supersonic channel flow, *J. Fluid Mech.* **509**, 207 (2004).
- [10] E. V. Driest, Turbulent boundary layer in compressible fluids, *J. Aeronaut. Sci.* **18**, 145 (1951).
- [11] S. E. Guarini, R. D. Moser, K. Shariff, and A. Wray, Direct numerical simulation of a supersonic turbulent boundary layer at Mach 2.5, *J. Fluid Mech.* **414**, 1 (2000).
- [12] L. Duan, I. Beekman, and M. Martin, Direct numerical simulation of hypersonic turbulent boundary layers. Part 3. Effect of Mach number, *J. Fluid Mech.* **672**, 245 (2011).
- [13] M. V. Morkovin, Effects of compressibility on turbulent flows, in *Mécanique de la Turbulence*, edited by A. Favre (CNRS, Paris, 1962), p. 367.
- [14] T. Maeder, Numerical investigation of supersonic turbulent boundary layers, Ph.D. thesis, ETH Zurich, 2000, doi: [10.3929/ethz-a-004015776](https://doi.org/10.3929/ethz-a-004015776).
- [15] Y.-S. Zhang, W.-T. Bi, F. Hussain, X.-L. Li, and Z.-S. She, Mach-Number-Invariant Mean-Velocity Profile of Compressible Turbulent Boundary Layers, *Phys. Rev. Lett.* **109**, 054502 (2012).
- [16] A. Trettel and J. Larsson, Mean velocity scaling for compressible wall turbulence with heat transfer, *Phys. Fluids* **28**, 026102 (2016).
- [17] A. Patel, J. W. Peeters, B. J. Boersma, and R. Pecnik, Semi-local scaling and turbulence modulation in variable property turbulent channel flows, *Phys. Fluids* **27**, 095101 (2015).
- [18] L. Sciacovelli, P. Cinnella, and X. Gloerfelt, Direct numerical simulations of supersonic turbulent channel flows of dense gases, *J. Fluid Mech.* **821**, 153 (2017).
- [19] M. M. Rai and P. Moin, Direct simulations of turbulent flow using finite-difference schemes, *J. Comput. Phys.* **96**, 15 (1991).
- [20] X.-L. Li, D.-X. Fu, Y.-W. Ma, and X. Liang, Direct numerical simulation of compressible turbulent flows, *Acta Mech. Sin.* **26**, 795 (2010).
- [21] J. Yao and F. Hussain, Supersonic turbulent boundary layer drag control using spanwise wall oscillation, *J. Fluid Mech.* **880**, 388 (2019).
- [22] M. Lee and R. D. Moser, Direct numerical simulation of turbulent channel flow up to  $Re_\tau \approx 5200$ , *J. Fluid Mech.* **774**, 395 (2015).
- [23] J. Kim, P. Moin, and R. Moser, Turbulence statistics in fully developed channel flow at low Reynolds number, *J. Fluid Mech.* **177**, 133 (1987).
- [24] S. Pirozzoli and M. Bernardini, Turbulence in supersonic boundary layers at moderate Reynolds number, *J. Fluid Mech.* **688**, 120 (2011).
- [25] A. Hadjadj, O. Ben-Nasr, M. Shadloo, and A. Chaudhuri, Effect of wall temperature in supersonic turbulent boundary layers: A numerical study, *Intl. J. Heat Mass Transf.* **81**, 426 (2015).
- [26] Z. S. She, X. Chen, and F. Hussain, Quantifying wall turbulence via a symmetry approach: A Lie group theory, *J. Fluid Mech.* **827**, 322 (2017).
- [27] B. J. Cantwell, A universal velocity profile for smooth wall pipe flow, *J. Fluid Mech.* **878**, 834 (2019).
- [28] S. Pirozzoli, Revisiting the mixing-length hypothesis in the outer part of turbulent wall layers: Mean flow and wall friction, *J. Fluid Mech.* **745**, 378 (2014).
- [29] B. Wu, W. Bi, F. Hussain, and Z.-S. She, On the invariant mean velocity profile for compressible turbulent boundary layers, *J. Turbul.* **18**, 186 (2017).
- [30] A. Walz, *Boundary Layers of Flow and Temperature* (MIT Press, Cambridge, MA, 1969).
- [31] Y.-S. Zhang, W.-T. Bi, F. Hussain, and Z.-S. She, A generalized Reynolds analogy for compressible wall-bounded turbulent flows, *J. Fluid Mech.* **739**, 392 (2014).
- [32] O. Reynolds, On the extent and action of the heating surfaces of steam boilers, *Proc. Manchester Lit. Phil. Soc* **14**, 7 (1874).
- [33] A. Busemann, *Handbuch der Experimentalphysik*, Vol. 4, Geest Portig (Akademische Verlagsgesellschaft, Leipzig, 1931).
- [34] L. Crocco, Sulla trasmissione del calore da una lamina piana a un fluido scorrente ad alta velocità, *L'Aerotecnica* **12**, 181 (1932).

- [35] S. Pirozzoli, F. Grasso, and T. Gatski, Direct numerical simulation and analysis of a spatially evolving supersonic turbulent boundary layer at  $M = 2.25$ , *Phys. Fluids* **16**, 530 (2004).
- [36] M. Bernardini, S. Pirozzoli, and P. Orlandi, Velocity statistics in turbulent channel flow up to  $Re_\tau = 4000$ , *J. Fluid Mech.* **742**, 171 (2014).
- [37] J. C. Del Alamo, J. Jiménez, P. Zandonade, and R. D. Moser, Scaling of the energy spectra of turbulent channels, *J. Fluid Mech.* **500**, 135 (2004).
- [38] I. Marusic, B. J. McKeon, P. A. Monkewitz, H. M. Nagib, A. J. Smits, and K. R. Sreenivasan, Wall-bounded turbulent flows at high Reynolds numbers: Recent advances and key issues, *Phys. Fluids* **22**, 065103 (2010).
- [39] A. Lozano-Durán and J. Jiménez, Effect of the computational domain on direct simulations of turbulent channels up to  $Re_\tau = 4200$ , *Phys. Fluids* **26**, 011702 (2014).
- [40] I. Marusic, W. J. Baars, and N. Hutchins, Scaling of the streamwise turbulence intensity in the context of inner-outer interactions in wall turbulence, *Phys. Rev. Fluids* **2**, 100502 (2017).
- [41] J. Jimenez and S. Hoyas, Turbulent fluctuations above the buffer layer of wall-bounded flows, *J. Fluid Mech.* **611**, 215 (2008).
- [42] K. R. Sreenivasan, *Turbulence Management and Relaminarization* (Springer-Verlag Berlin, Heidelberg, 1988).
- [43] X. Chen, F. Hussain, and Z.-S. She, Non-universal scaling transition of momentum cascade in wall turbulence, *J. Fluid Mech.* **871**, R2 (2019).
- [44] H. Abe and R. A. Antonia, Relationship between the energy dissipation function and the skin friction law in a turbulent channel flow, *J. Fluid Mech.* **798**, 140 (2016).
- [45] R. Monaghan, *A Review and Assessment of Various Formulae for Turbulent Skin Friction in Compressible Flow* (Aeronautical Research Council, Citeseer, 1953).
- [46] P. Huang, P. Bradshaw, and T. Coakley, Skin friction and velocity profile family for compressible turbulent boundary layers, *AIAA J.* **31**, 1600 (1993).
- [47] W. Li, Y. Fan, D. Modesti, and C. Cheng, Decomposition of the mean skin-friction drag in compressible turbulent channel flows, *J. Fluid Mech.* **875**, 101 (2019).
- [48] K. Fukagata, K. Iwamoto, and N. Kasagi, Contribution of Reynolds stress distribution to the skin friction in wall-bounded flows, *Phys. Fluids* **14**, L73 (2002).
- [49] T. Gomez, V. Flutet, and P. Sagaut, Contribution of Reynolds stress distribution to the skin friction in compressible turbulent channel flows, *Phys. Rev. E* **79**, 035301(R) (2009).
- [50] Z. Chen, C. P. Yu, L. Li, and X. L. Li, Effect of uniform blowing or suction on hypersonic spatially developing turbulent boundary layers, *Sci. China: Phys., Mech. Astron.* **59**, 664702 (2016).
- [51] M. Yu, C.-X. Xu, and S. Pirozzoli, Genuine compressibility effects in wall-bounded turbulence, *Phys. Rev. Fluids* **4**, 123402 (2019).
- [52] J. Yao, X. Chen, and F. Hussain, Reynolds number effect on drag control via spanwise wall oscillation in turbulent channel flows, *Phys. Fluids* **31**, 085108 (2019).
- [53] Y. Fan, C. Cheng, and W. Li, Effects of the Reynolds number on the mean skin friction decomposition in turbulent channel flows, *Appl. Math. Mech.* **40**, 331 (2019).
- [54] N. Renard and S. Deck, A theoretical decomposition of mean skin friction generation into physical phenomena across the boundary layer, *J. Fluid Mech.* **790**, 339 (2016).
- [55] J. Jiménez, Cascades in wall-bounded turbulence, *Annu. Rev. Fluid Mech.* **44**, 27 (2012).
- [56] W. J. Baars and I. Marusic, Data-driven decomposition of the streamwise turbulence kinetic energy in boundary layers. Part 1. Energy spectra, *J. Fluid Mech.* **882**, A25 (2020).
- [57] W. Schoppa and F. Hussain, Coherent structure generation in near-wall turbulence, *J. Fluid Mech.* **453**, 57 (2002).
- [58] F. Waleffe, On a self-sustaining process in shear flows, *Phys. Fluids* **9**, 883 (1997).
- [59] J. Yao, X. Chen, and F. Hussain, Drag control in wall-bounded turbulent flows via spanwise opposed wall-jet forcing, *J. Fluid Mech.* **852**, 678 (2018).
- [60] I. Marusic, R. Mathis, and N. Hutchins, Predictive model for wall-bounded turbulent flow, *Science* **329**, 193 (2010).

- [61] Y. Hwang, Statistical structure of self-sustaining attached eddies in turbulent channel flow, *J. Fluid Mech.* **767**, 254 (2015).
- [62] N. Hutchins and I. Marusic, Evidence of very long meandering features in the logarithmic region of turbulent boundary layers, *J. Fluid Mech.* **579**, 1 (2007).
- [63] L. Agostini and M. Leschziner, On the influence of outer large-scale structures on near-wall turbulence in channel flow, *Phys. Fluids* **26**, 075107 (2014).
- [64] J. Hwang and H. J. Sung, Influence of large-scale motions on the frictional drag in a turbulent boundary layer, *J. Fluid Mech.* **829**, 751 (2017).
- [65] J. Yao and F. Hussain, Toward vortex identification based on local pressure-minimum criterion in compressible and variable density flows, *J. Fluid Mech.* **850**, 5 (2018).
- [66] R. J. Adrian, Hairpin vortex organization in wall turbulence, *Phys. Fluids* **19**, 041301 (2007).
- [67] P. Schlatter, Q. Li, R. Örlü, F. Hussain, and D. S. Henningson, On the near-wall vortical structures at moderate Reynolds numbers, *Eur. J. Mech.-B* **48**, 75 (2014).
- [68] J. Jiménez, Coherent structures in wall-bounded turbulence, *J. Fluid Mech.* **842**, P1 (2018).
- [69] L. Zhu and L. Xi, Vortex axis tracking by iterative propagation (VATIP): A method for analysing three-dimensional turbulent structures, *J. Fluid Mech.* **866**, 169 (2019).
- [70] B. Ganapathisubramani, N. Hutchins, J. Monty, D. Chung, and I. Marusic, Amplitude and frequency modulation in wall turbulence, *J. Fluid Mech.* **712**, 61 (2012).
- [71] J. Yao, Compressible turbulent channel flow, Texas Data Repository Dataverse, 2020, <https://doi.org/10.18738/T8/OIXQTG>.